

GT2010-22984

## COMPUTATIONAL PREDICTIONS OF HEAT TRANSFER AND FILM-COOLING FOR A TURBINE BLADE WITH NON-AXISYMMETRIC ENDWALL CONTOURING

Stephen P. Lynch  
Karen A. Thole

Mechanical and Nuclear Engineering Department  
The Pennsylvania State University  
University Park, PA 16802, USA

Atul Kohli  
Christopher Lehane

Pratt & Whitney  
400 Main Street  
East Hartford, CT 06108, USA

### ABSTRACT

Three-dimensional contouring of the compressor and turbine endwalls in a gas turbine engine has been shown to be an effective method of reducing aerodynamic losses by mitigating the strength of the complex vortical structures generated at the endwall. Reductions in endwall heat transfer in the turbine have been also previously measured and reported in the literature. In this study, computational fluid dynamics simulations of a turbine blade with and without non-axisymmetric endwall contouring were compared to experimental measurements of the exit flowfield, endwall heat transfer and endwall film-cooling. Secondary kinetic energy at the cascade exit was closely predicted with a simulation using the SST  $k-\omega$  turbulence model. Endwall heat transfer was overpredicted in the passage for both the SST  $k-\omega$  and realizable  $k-\epsilon$  turbulence models, but heat transfer augmentation for a non-axisymmetric contour relative to a flat endwall showed fair agreement to the experiment. Measured and predicted film-cooling results indicated that the non-axisymmetric contouring limits the spread of film-cooling flow over the endwall depending upon the interaction of the film with the contour geometry.

### INTRODUCTION

Vortical secondary flows near the airfoil-endwall junction in an axial turbine are responsible for reduced aerodynamic efficiency and high heat transfer rates. Furthermore, the sweeping action of the flows can displace coolant ejected through holes in the part, which normally provides a film of cool air to shield the part from hot gas temperatures. This complex flowfield near the endwall is difficult to accurately model with current computational methods, and improvement in modeling fidelity is important to achieve further gains in turbine efficiency and durability.

The potential for efficiency and durability improvement using computational fluid dynamics (CFD) simulations is illustrated by the development of non-axisymmetric (three-dimensional) contouring designs for turbine endwalls. Three-

dimensional variation of the endwall surface has been generally determined through an optimization routine coupled to three-dimensional Reynolds-Averaged Navier Stokes (RANS) simulations. Experimental validations of the resulting shapes have demonstrated reductions in the strength of vortical secondary flows and improvements in turbine efficiency.

Although current computational methods are adequate to produce optimized endwall designs, predictions rarely capture all of the improvements demonstrated by experiments. A complete turbine design also must consider the full aerodynamic and thermal environment. The motivation for this paper is to examine the validity of RANS-based modeling for non-axisymmetric contour design through comparison to measured flowfields, endwall heat transfer, and film cooling effectiveness.

### NOMENCLATURE

BL	boundary layer
C	true chord of blade
$C_{ax}$	axial chord of blade
$C_p$	specific heat at constant pressure, or static pressure coefficient, $C_p = (P_s - P_{s,in}) / (0.5\rho\bar{U}_{\infty,in}^2)$
$C_{Ptot}$	total pressure loss coefficient, $C_{Ptot} = (P_{tot} - P_{tot,\infty,in}) / (0.5\rho\bar{U}_{\infty,in}^2)$
$C_{SKE}$	secondary kinetic energy coefficient, $C_{SKE} = (\bar{V}_n^2 + \bar{V}_z^2) / \bar{U}_{\infty,in}^2$
d	film-cooling hole diameter
h	heat transfer coefficient, $h = q''_w / (T_w - T_{\infty,in})$
H	boundary layer shape factor
k	thermal conductivity, or turbulent kinetic energy
L	film-cooling hole length
$\dot{m}$	mass flow rate
$M_{ideal}$	ideal (lossless) blowing ratio, see Eq. 1
$\bar{M}_{ideal}$	average ideal blowing ratio, see Eq. 2
N	total number of film holes

Nu	Nusselt number, $Nu = hC_{ax}/k_{air}$
P	blade pitch
$P_s$	static pressure
$P_{tot}$	total pressure
$q''_w$	wall heat flux
$Re_s$	boundary layer Reynolds number, $Re_s = s\bar{U}_\infty/\nu$
$Re_\theta$	momentum thickness Reynolds number, $Re_\theta = \theta\bar{U}_\infty/\nu$
s	streamwise distance along maximum film effectiveness, or distance downstream of start of BL
S	blade span
SST	Shear Stress Transport
St	Stanton number, $St = h/\rho C_p \bar{U}_\infty$
T	temperature
$T_{back}$	average background temperature associated with radiation reflected off a surface from its surroundings
Tu	freestream turbulence intensity
X, Y, Z	global coordinates, where X is blade axial direction
U, V, W	velocity components aligned with global coordinates
$\bar{U}$	streamwise velocity
$V_n$	pitchwise component of mean velocity on a plane normal to the mass-averaged velocity vector, $V_n = -U \sin(\bar{\alpha}) + V \cos(\bar{\alpha})$
$V_z$	spanwise component of mean velocity on a plane normal to the mass-averaged velocity vector, $V_z = W$

### Greek

$\bar{\alpha}$	mass-averaged yaw angle
$\delta_{99}$	boundary layer thickness (99%)
$\varepsilon$	emissivity, or turbulent dissipation
$\eta$	adiabatic effectiveness, $\eta = (T_\infty - T_{aw})/(T_\infty - T_c)$
$\bar{\eta}$	laterally averaged adiabatic effectiveness
$\theta$	momentum thickness
$\nu$	kinematic viscosity
$\rho$	density
$\omega$	specific dissipation, $\omega \propto \varepsilon/k$

### Subscripts/Superscripts

aw	adiabatic wall conditions
exit	exit conditions
c	coolant conditions
in	inlet conditions
k	k-th film cooling hole
max	maximum value
w	wall conditions
$\infty$	local freestream conditions

### **RELEVANT PAST STUDIES**

The complex shape of a non-axisymmetric contoured endwall is typically generated through a geometric optimization coupled to a three-dimensional CFD code. An example of the power of this method was presented by Harvey et al. [1]. Their optimal design was based on reducing the cross-passage

pressure gradient and exit flow angle deviation. Significant reductions in secondary kinetic energy and flow angle deviation with contouring were predicted relative to the baseline flat endwall. Experimental validation by Hartland et al. [2] demonstrated the reduction in secondary kinetic energy, but also found an improvement in loss not predicted by Harvey et al. [1]. Nagel and Baier's [3] optimization of the endwall and airfoil of a low-pressure turbine blade resulted in reasonably close predictions of loss for the optimized shape.

Germain et al. [4] used a 3D RANS code to design endwall contours for the stator and rotor of a 1 1/2 stage rotating turbine. Although secondary kinetic energy agreed well with experiments of Schuepbach et al. [5], overall turbine efficiency improvement with contouring was underpredicted.

A series of studies have been performed to analyze the usefulness of endwall contouring in a family of highly loaded low pressure turbine blades. Praisner et al. [6] presented a computational optimization methodology for a baseline Pack-B low pressure airfoil and two related highly-loaded designs. Loss reduction was a primary metric in the optimization. Flowfield measurements of the resulting geometries by Knezevici et al. ([7], [8]) demonstrated reduced loss and secondary kinetic energy compared to a flat endwall.

Saha and Acharya [9] used endwall heat transfer as the optimization metric for a contour design. Significant reductions in heat transfer were predicted near the suction side leading edge and in the throat, relative to a flat endwall. Measurements of the contour by Mahmood et al. [10] did not reproduce the same magnitude of heat transfer reduction, but heat transfer augmentation due to the passage vortex and the suction side leg of the horseshoe vortex were reduced. Lynch et al. [11] measured endwall heat transfer for the contour design studied by Praisner et al. [6] and Knezevici et al. [7]. Relative to a flat endwall, the contour increased heat transfer near the saddle point but reduced heat transfer near the pressure side-endwall junction, which was considered more significant since flat endwall heat transfer levels were high in that region.

Film-cooling for non-axisymmetric endwall contours was considered in a computational study by Okita and Nakamata [12]. A reduction in passage vortex strength with contouring allowed the coolant to remain closer to the endwall in the downstream portion of the passage. Flowfield measurements were performed by Gustafson et al. [13] for full-coverage film cooling on the contour of Saha and Acharya [9]. Gustafson et al. [13] concluded that coolant jets stay close to the surface, although overall cascade loss (including losses through the holes) increased with blowing ratio. Increases in blowing ratio for the same film-cooled contour resulted in higher film effectiveness and reduced near-wall overturning, in the study of Mahmood et al. [14].

The computational predictions reported here simulated the flat and non-axisymmetric geometries studied by Knezevici et al. [7] and Lynch et al. [11]. Also included in this paper are experimental measurements and computational predictions of film-cooling for the flat and contoured endwalls.

## COMPUTATIONAL METHODOLOGY

Simulations of the flat and contoured endwall geometries studied by Knezevici et al. [7] and Lynch et al. [11] were performed using the commercial computational fluid dynamics software FLUENT [15]. The pressure-based formulation of the steady Reynolds-Averaged Navier-Stokes equations (RANS), the turbulence closure equations, and the energy equation were solved with second-order discretization of all variables. The SST  $k-\omega$  turbulence model [16] was chosen for closure of the RANS equations. This model has shown reasonable agreement with experimental results in turbomachinery applications ([17], [18]). The realizable  $k-\epsilon$  turbulence model [19] has also shown reasonable agreement with experimental heat transfer data ([20], [21], [22]), and predictions with this model are also considered.

The experimental setup described in Lynch et al. [11] included a heater on the endwall that extended  $3.32C_{ax}$  upstream of the blade (along the streamwise direction). To capture the development of the endwall heat transfer upstream of the cascade, the computational grid extended  $4.3C_{ax}$  upstream of the blade leading edge, as shown in Figure 1a. A velocity inlet with a boundary layer profile benchmarked to the experiment was set at this location; see benchmarking details in a later section. Periodic boundaries were employed on the sides of the domain, and an outflow boundary extended  $1.5C_{ax}$  downstream of the blade trailing edge. A symmetry boundary condition was applied at midspan. For heat transfer studies, a uniform heat flux boundary condition was imposed on the endwall, starting at  $3.32C_{ax}$  upstream of the blade and extending to the domain exit. All other surfaces were modeled as adiabatic, as per the experiment. For the film cooling cases, all surfaces were modeled as adiabatic.

The commercial grid generation program ICFM [23] was used to create multi-block structured grids for the flat and

contoured endwall geometries. The initial grid size for the heat transfer studies was 1.2 million cells, with grid spacing refined near walls such that  $y^+$  was less than 1 everywhere. Refer to Figure 1b-c for a depiction of the flat and contoured endwall grids in the passage. For the film-cooling predictions, the same multi-block format was used, with O-grids created around each of the film-cooling holes. Figure 2 depicts the flat and contoured endwall grids. A plenum was added below the endwall to feed the cooling holes. The dimensions of the plenum relative to the hole diameter are also shown. A more detailed description of the hole geometry is presented later.

Convergence of a simulation was determined through the following three ways: normalized residuals had to reach values lower than  $10^{-4}$  ( $10^{-6}$  for energy); area-averaged endwall Nusselt number (for heat transfer cases) or area-averaged endwall film effectiveness (for film-cooling cases) had to change by less than 0.1% over 500 iterations; and mass-averaged total pressure over a plane located  $1.4C_{ax}$  downstream of the blade leading edge had to change by less than 0.1% over 500 iterations.

Grid independence for the heat transfer cases was determined by refining and coarsening the mesh relative to the nominal mesh size of 1.7 million cells. The difference in area-averaged Nu over the endwall varied by less than 1% for the coarse grid (0.68 million cells) and the refined grid (3.17 million cells), relative to the nominal grid. Mass-averaged total pressure over the plane located  $1.4C_{ax}$  downstream of the blade leading edge also varied by less than 0.6% for the coarse and refined grids, relative to the nominal grid. Based on these results, the nominal grid size was considered to be sufficient for heat transfer and flowfield predictions.

The solution-based grid adaption capability in FLUENT was used to check grid independence for the film-cooling studies by refining the mesh based on gradients of temperature.

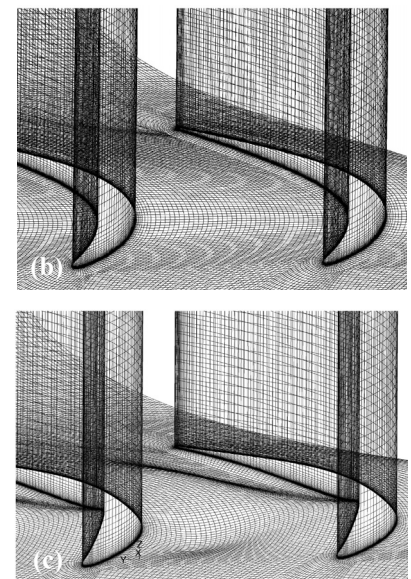
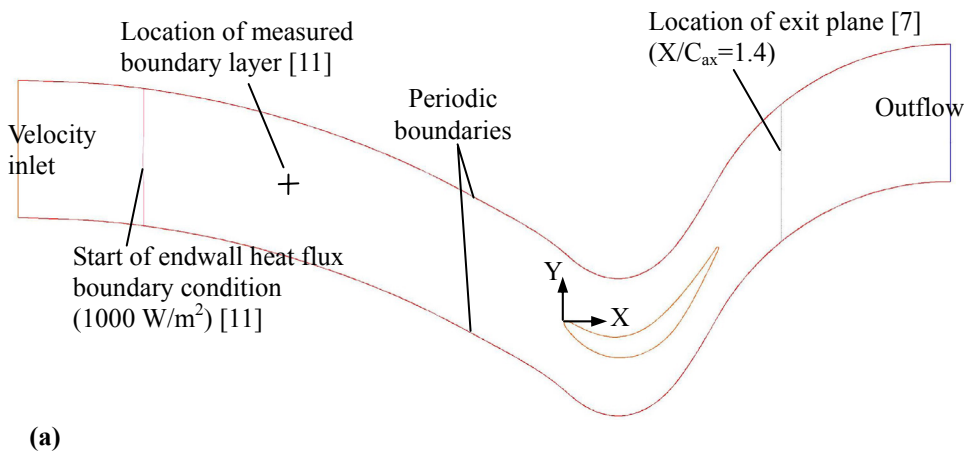


**Figure 1. Depictions of (a) the computational domain and boundary conditions; (b) the flat endwall grid; and (c) the contoured endwall grid.**

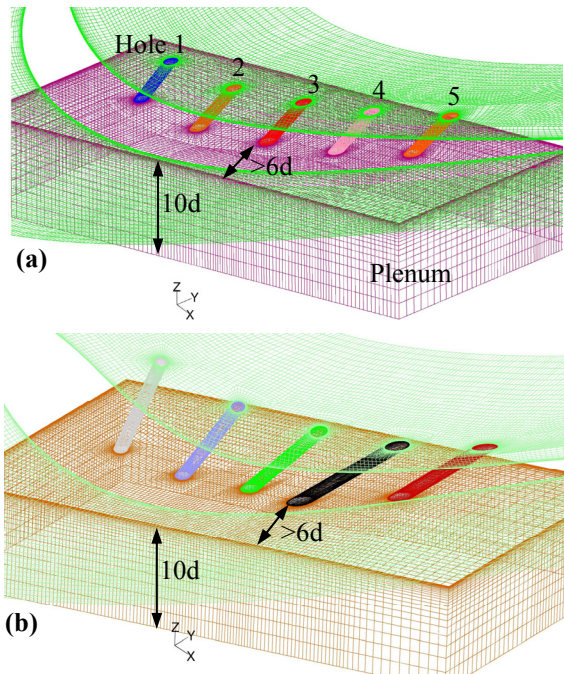


**Figure 2. Depiction of (a) the flat endwall film-cooling grid and hole nomenclature; and (b) the contoured endwall film-cooling grid.**

For each film-cooling flowrate, the baseline converged mesh (2.8 million cells) was initially refined to reduce the gradient in temperature by 20%, which added nominally 250,000 cells. The case was then run again to convergence. A second refining adaption resulted in a final mesh size of approximately 3.5 million cells. Area-averaged effectiveness increased by about 1% for the first refinement relative to the baseline grid, and increased further by 0.2% for the second refinement relative to the first. Results from the largest grid are reported here.

### Benchmarking of Inlet Conditions

Lynch et al. [11] made measurements of the inlet boundary layer at a location  $2.85C_{ax}$  upstream of the blade leading edge along the direction of the inlet velocity ( $2.33C_{ax}$  in the axial direction). As noted earlier, the computational grid inlet was placed upstream of that location. The boundary layer code TEXSTAN [24] was used to generate profiles of velocity, turbulent kinetic energy, and turbulent dissipation for the grid

inlet, such that the measured boundary layer and endwall heat transfer development downstream of the start of the endwall heater were duplicated in the FLUENT simulations. The dissipation profile from TEXSTAN was converted to specific dissipation for the SST  $k-\omega$  model using the relationship outlined in Menter [16].

Figure 3 compares the measured boundary layer to a prediction using TEXSTAN, and to results from the FLUENT simulations using inlet profiles generated by TEXSTAN. All of the predictions agree well with the measured boundary layer. See Table 1 for a comparison of the boundary layer parameters for the various predictions, and a comparison to the measured boundary layer parameters of Knezevici et al. [7]. The boundary layer thickness in the simulation is slightly smaller than that of Knezevici et al. [7], but was deemed reasonably close for comparison.

The development of the endwall heat transfer upstream of the blade cascade along the streamwise direction is shown in Figure 4. Note that  $Re_s$  for each data set is referenced to its respective virtual origin. Both the trend and the magnitude of measured endwall heat transfer are well-predicted by the FLUENT simulation, and both match the expected behavior from the unheated starting length correlation of Kays and Crawford [25].

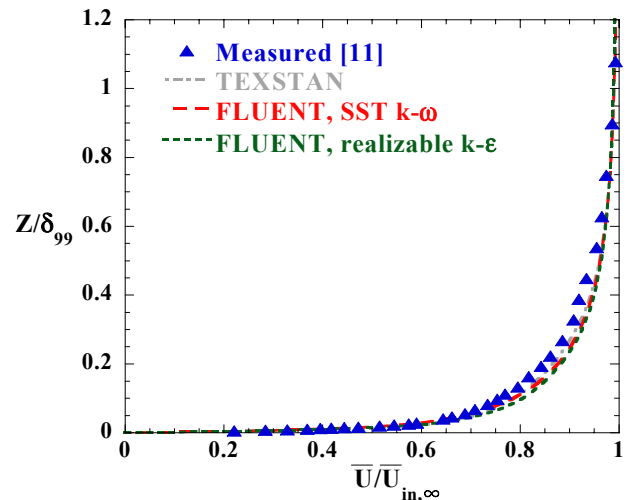


**Figure 3. Measurement [11] and predictions of the boundary layer at  $X/C_{ax} = -2.33$  upstream of the blade.**

**Table 1 Comparison of Inlet Boundary Conditions**

	Lynch, et al. [11]	TEXSTAN	FLUENT, SST $k-\omega$	FLUENT, realizable $k-\epsilon$	Knezevici, et al. [7]	FLUENT, SST $k-\omega$
$C_{ax}$ [mm]	218.4	218.4	218.4	218.4	75.4	218.4
$S$ [mm]	546	546	546	546	203.2	546
Measurement location (axial)	$-2.33C_{ax}$	$-2.33C_{ax}$	$-2.33C_{ax}$	$-2.33C_{ax}$	$-1.2C_{ax}$	$-1.2C_{ax}$
$\delta_{99}/S$	0.061	0.066	0.069	0.074	0.095	0.085
$\theta/S$	0.0046	0.0046	0.0046	0.0047	0.0079	0.0058
$Re_0$	1330	1330	1330	1340	2660	1670
$H$	1.3	1.3	1.3	1.3	1.2	1.3
$Tu$	6%	6%	6%	6%	4%	6%

Blade surface static pressures at midspan were compared to the measurements of Lynch et al. [11] to confirm proper blade loading for the simulations. Figure 5 shows blade static pressure, non-dimensionalized as a pressure coefficient. Both turbulence model cases demonstrated good agreement to measurements. Note that the high aspect ratio of the blade and the relatively modest contouring resulted in the same loading at midspan for the flat and contoured endwall geometries.

### FILM COOLING MEASUREMENTS

Measurements of film cooling effectiveness were obtained in a large-scale low-speed test section that could be fitted with a flat or a three-dimensionally contoured endwall. The geometry, benchmarking, and endwall heat transfer measurement method were presented previously by Lynch et al. [11]; thus, only a brief overview of those topics is given here.

A large low-speed wind tunnel provided flow through a scaled low-pressure turbine blade cascade. The wind tunnel,

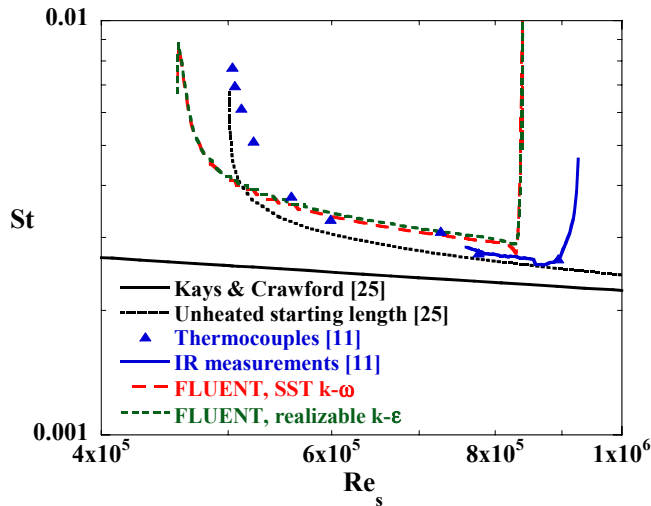


Figure 4. Measurements [11] and predictions of the endwall heat transfer upstream of the cascade.

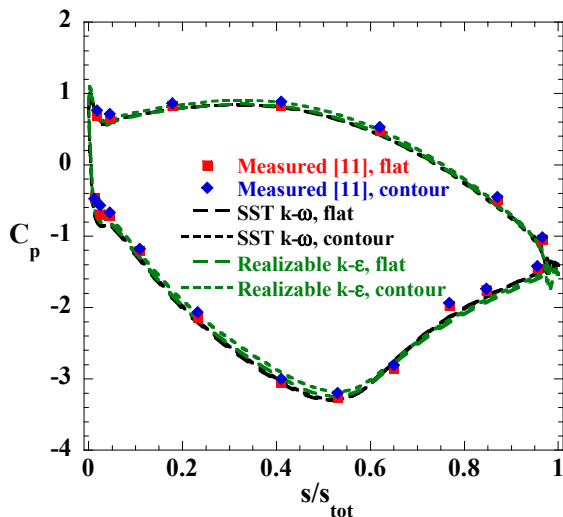


Figure 5. Measured [11] and predicted blade surface static pressure at midspan.

depicted in Figure 6, has the capability to create a temperature differential between the mainstream and the coolant air by heating the former with a 55 kW electric heater bank, and cooling the latter with a 40 kW chiller. For the film-cooling measurements presented here, a temperature differential of at least 20°C was maintained, with the coolant nominally at 23°C. This resulted in a coolant-to-mainstream density ratio of approximately 1.06. The benchmarking and heat transfer studies in Lynch et al. [11] required no heating or cooling.

The rectilinear blade test section contained seven low-pressure turbine blades based on the Pack-B midspan airfoil geometry. This geometry has been presented in several studies in the literature, on topics ranging from active flow control ([26], [27]), to benchmarking with higher-loaded designs ([28], [29]), to the optimization and measured performance of three-dimensional endwall contouring ([6], [7]). See Table 2 for a summary of the test section geometry and flow parameters. The contour endwall shape consisted of a peak near the pressure side of the airfoil and a depression near the suction side in the forward part of the passage, and a ridge through the passage from the pressure to suction side (see Figure 1c).

Adiabatic film cooling effectiveness was measured for the flat and three-dimensionally contoured endwalls by capturing the steady-state endwall temperature with an infrared camera. Coolant was ejected onto the endwall through discrete holes located near the blade pressure side. The flat and contoured

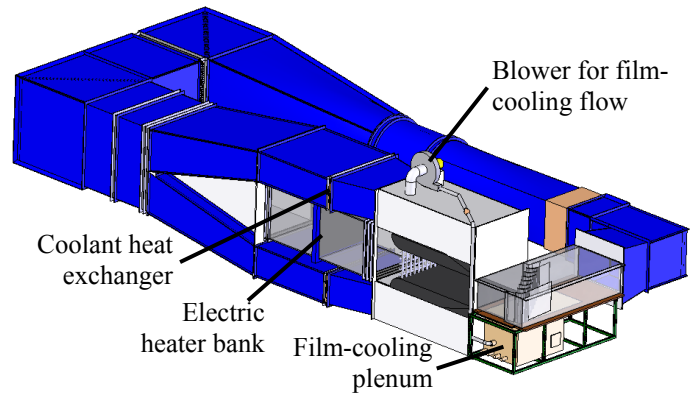


Figure 6. Depiction of the large-scale low-speed wind tunnel, with piping for the film-cooling studies.

Table 2 Blade Geometry and Flow Conditions

Number of blades	7
Scale factor	8.6
Axial chord ( $C_{ax}$ )	0.218 m
True chord ( $C$ )	0.241 m
Pitch/chord ( $P/C_{ax}$ )	0.826
Span/chord ( $S/C_{ax}$ )	2.50
Inlet Re ( $Re_{in} = C_{ax} \bar{U}_{\infty, in} / \nu$ )	$1.25 \times 10^5$
Exit Re ( $Re_{exit} = C_{ax} \bar{U}_{\infty, exit} / \nu$ )	$2.00 \times 10^5$
Inlet velocity ( $\bar{U}_{\infty, in}$ )	8.7 m/s
Inlet, exit design flow angles	35°, 60°
Inlet, exit Mach	0.026, 0.042

endwalls were constructed of low thermal conductivity foam ( $k \approx 0.03$  W/m-K) for minimal conduction losses. The flat endwall foam was uniformly 12.7 mm thick. A two-part expanding foam cast in a mold was used to model the shape of the three-dimensional contour.

The endwall surfaces were painted flat black for high emissivity and resolution in IR measurements. An IR camera with 240x320 pixel resolution (spatial integration of 0.16d) was used to capture images at each of several locations over the entire endwall. The average of five images at a location was then calibrated for emissivity and background temperature by comparison to embedded thermocouples in the endwall. Typical values for emissivity and background temperature were  $\epsilon = 0.92$  and  $T_{\text{back}} = 50^\circ\text{C}$ , which compared well to published emissivity for black paint ( $\epsilon = 0.94$ ) and the measured freestream temperature ( $T_\infty = 46^\circ\text{C}$ ). The resulting calibrated images were assembled into a temperature map of the endwall and converted to film effectiveness ( $\eta$ ) using measured freestream and coolant plenum temperatures.

Five cylindrical holes ( $d/C_{\text{ax}} = 0.020$ ) were spaced evenly near the airfoil pressure side-endwall junction, in a region of high heat transfer seen in the flat endwall heat transfer measurements. Hole locations were kept consistent relative to the blade for both the flat and contoured endwall studies as shown in Figure 2. Injection angles for the flat endwall holes were aligned with the direction of flat endwall streaklines from the oil flow visualization reported in Lynch et al. [11]. It was considered that since the holes were so close to the airfoil, the surface inclination angle in a manufactured part would be limited so that the film hole can be fed from below the blade platform. To accommodate this limitation, the surface inclination angle for the flat endwall holes was  $40^\circ$ , except for hole 1 which had a surface inclination angle of  $45^\circ$ . The  $L/d$  ratio of the flat endwall film holes was 4.1.

The same coolant feed limitation was considered for the contoured endwall due to the varying thickness and surface orientation of the three-dimensional endwall. Because of this, holes 1 and 2 near the peak of the endwall contour had surface inclination angles of  $80^\circ$  and  $60^\circ$ , respectively. Holes 3-5 had more modest surface inclination angles, ranging from  $45^\circ$  to  $30^\circ$ . In keeping with the methodology of the flat endwall, the injection directions for the contoured endwall were aligned with streaklines for that geometry. Lynch et al. [11] noted that the endwall streaklines originating from the pressure side of the passage were less directed toward the suction side for the contoured endwall; thus, injection angles were slightly different than those of the flat endwall.  $L/d$  ratios for the contoured endwall holes ranged from 7 to 8.5.

Film-cooling flowrates were characterized by averaging the ideal blowing ratio (based on inviscid local velocities) for each hole to obtain a global average  $\overline{M}_{\text{ideal}}$ . The ideal blowing ratio for each hole was determined through measurements of the plenum total pressure and the local endwall static pressure, where local endwall static pressure was measured in an

adjacent passage without film cooling. The calculation of an individual hole's ideal blowing ratio was:

$$M_{\text{ideal}} = \frac{(\rho U)_c}{(\rho U)_{\infty, \text{local}}} = \sqrt{\frac{\rho_c}{\rho_\infty} \left( \frac{P_{o, \text{plen}} - P_{s, \text{endwall}}}{P_{o, \text{in}} - P_{s, \text{endwall}}} \right)} \quad (1)$$

The average ideal blowing ratio of all five holes was then determined and used to characterize the leakage:

$$\overline{M}_{\text{ideal}} = \sum_{k=1}^N M_{\text{ideal}, k} / N \quad (2)$$

This method for calculating ideal blowing ratio was also used to set the mass flow inlet conditions for the coolant plenum in the computational studies. The predicted mass flow rates into the plenum (as a percent of mainstream mass flow) at each ideal average blowing ratio in this study are listed in Table 3.

Uncertainty in adiabatic film cooling measurements was estimated with the partial derivative method of Moffat [30]. The largest contribution to uncertainty was the surface temperature measurement with the IR camera, which had a bias error of  $0.6^\circ\text{C}$  and a precision error of  $0.2^\circ\text{C}$ . Total uncertainty in adiabatic film cooling effectiveness was estimated to be  $\partial\eta = \pm 0.04$  at a value of  $\eta = 0.3$ .

## RESULTS AND DISCUSSION

Steady 3D RANS predictions for a flat and a contoured endwall were compared to experimental results. Flowfield validation is followed by comparisons to endwall heat transfer. Finally, measured film-cooling effectiveness with and without a contour is discussed and the resulting predictions are analyzed.

### Cascade Exit Flowfield Predictions

A comparison of planar measurements (Knezevici et al. [7]) and computational predictions for the flat and contoured endwalls (from the grids without film-cooling) is shown in Figure 7. The measurement plane is located at  $X/C_{\text{ax}} = 1.4$  downstream of the blade leading edge (see Figure 1). In Figure 7, line contours of total pressure loss coefficient ( $C_{\text{Ptot}}$ ) are overlaid on flood contours of secondary kinetic energy coefficient ( $C_{\text{SKE}}$ ). Comparisons of Figure 7a to 7b indicate good agreement between measured and predicted  $C_{\text{SKE}}$  with the SST  $k-\omega$  turbulence model for the flat endwall. The only exception is an underprediction of the magnitude of  $C_{\text{SKE}}$  very close to the endwall ( $Z/S < 0.05$ ). The predicted total pressure loss coefficient contours in Figure 7b show similar trends to the measurements in Figure 7a, especially in capturing the two distinct loss cores between  $0.1 < Z/S < 0.2$ . The predicted magnitudes of  $C_{\text{Ptot}}$  are higher, however, particularly in the loss

**Table 3 Ideal Blowing Ratios and Flowrates**

	$\overline{M}_{\text{ideal}}$	$\dot{m}_c / \dot{m}_\infty$ (from CFD)
Flat	1.0	0.038%
Flat	2.0	0.088%
Contour	1.0	0.038%
Contour	2.0	0.088%

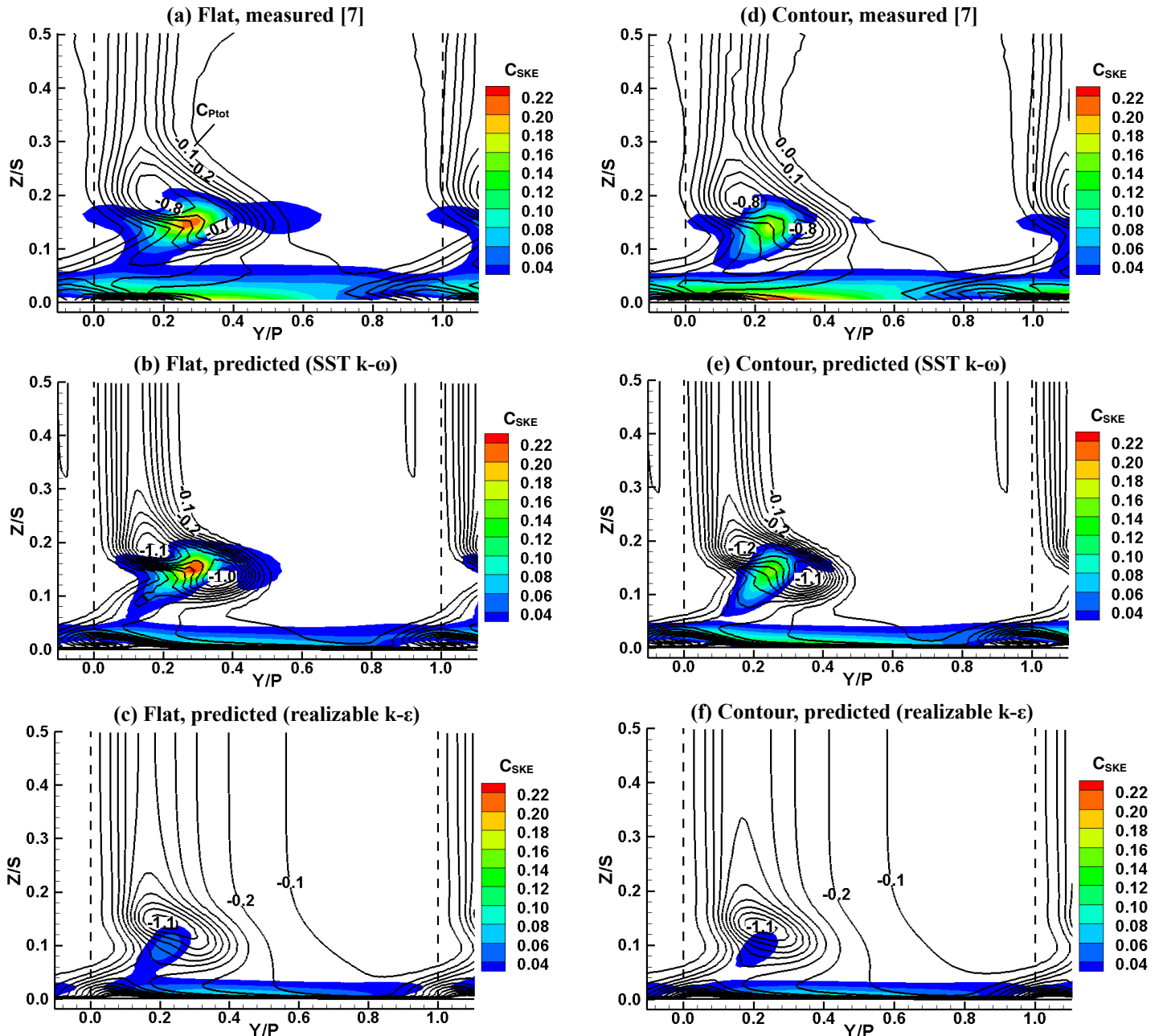


**Figure 7. Line contours of  $C_{p,tot}$  overlaid with flood contours of  $C_{SKE}$  at  $X/C_{ax}=1.4$ , for the flat endwall (a-c) and the contoured endwall (d-f).**

cores and in the blade wake. While the difference might be partially due to limited spatial resolution in the experiment, it has also been shown that eddy-viscosity turbulence models tend to overpredict both secondary and midspan blade wake losses ([31]).

The flat endwall predictions using the realizable  $k-\epsilon$  turbulence model (Figure 7c) show poor agreement for both  $C_{SKE}$  and  $C_{p,tot}$  when compared to the measurements in Figure 7a. The peak magnitude of secondary kinetic energy is underpredicted and shifted closer to the endwall. There is a gross overprediction of the blade wake near midspan

( $Z/S=0.5$ ), compared to the measurement. Also, the two distinct loss cores seen in the measurements are not apparent in the prediction in Figure 6c, which shows only a single loss core.

Knezevici et al. [7] attributed the reduction in  $C_{SKE}$  and  $C_{p,tot}$  for the contoured endwall (Figure 7d) versus the flat endwall (Figure 7a) to reduced pitchwise cross-flow in the passage. This in turn weakened the passage vortex and reduced associated losses. The blending of the contour back to a flat wall at the trailing edge plane of the cascade increased pitchwise cross-flow, however, which is indicated by the higher near-wall  $C_{SKE}$  in Figure 7d. The prediction for the contoured

endwall using the SST  $k-\omega$  model (Figure 7e) shows good agreement for  $C_{SKE}$  but, as was seen for the flat endwall, continues to overpredict  $C_{Ptot}$  in the loss cores and the blade profile loss. Overall, the measured trends between the flat and contoured endwalls appear to be well-replicated by the use of the SST  $k-\omega$  model, even if  $C_{Ptot}$  magnitudes are not. The realizable  $k-\epsilon$  model (Figure 7f) again results in poor predictions. Interestingly, a predicted 30 percent reduction in the peak  $C_{SKE}$  between Figures 7c and 7f compares reasonably to the measured percent reduction of approximately 24%, suggesting that perhaps trends between the flat and contoured endwall are being correctly predicted.

Figures 8 and 9 compare spanwise distributions of  $C_{SKE}$  and  $C_{Ptot}$  extracted from the measured and predicted flowfields. In Figure 8,  $C_{SKE}$  distributions are plotted at  $Y/P=0.3$ , which passes through the peak of secondary kinetic energy

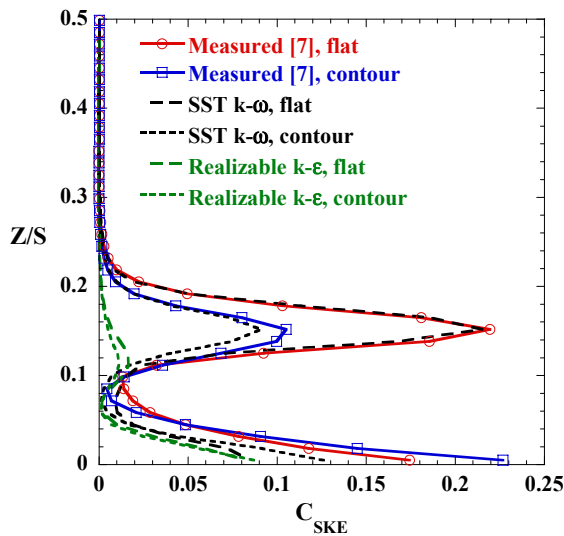


Figure 8. Comparison of measured [7] and predicted  $C_{SKE}$ , extracted from Figure 7 at  $Y/P=0.3$ .

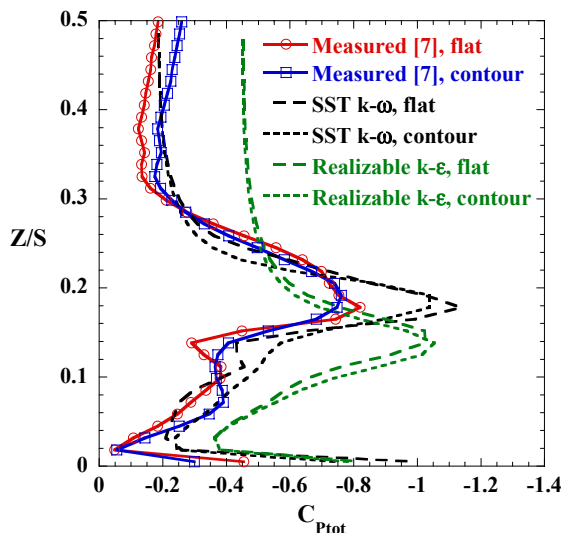


Figure 9. Comparison of measured [7] and predicted  $C_{Ptot}$ , extracted from Figure 7 at  $Y/P=0.2$ .

coefficient. The SST  $k-\omega$  model prediction demonstrates very good agreement in peak  $C_{SKE}$  at  $Z/S=0.15$  for the flat endwall, but underpredicts  $C_{SKE}$  below  $Z/S=0.08$ . The contoured endwall prediction with the SST  $k-\omega$  model is not quite as good around the peak  $C_{SKE}$  as for the flat endwall, suggesting some physics of the contouring may not be as well captured. The realizable  $k-\epsilon$  model does not reproduce the location or magnitude of the peak  $C_{SKE}$  for the flat or contoured endwall.

The spanwise distribution of  $C_{Ptot}$  in Figure 9 is taken at  $Y/P=0.2$ , which passes through the peak of the leftmost total pressure loss core in Figures 7a-f. As noted earlier, neither turbulence model correctly captured the magnitude of total pressure loss cores; however, the SST  $k-\omega$  model predicts the peak  $C_{Ptot}$  to occur at the same location in the flowfield ( $Z/S=0.17$ ) as indicated by the measurements. In contrast, the realizable  $k-\epsilon$  predicts the total pressure loss peak to occur at  $Z/S=0.14$ .

The difference in prediction accuracy between the two turbulence models examined here seems to have important implications for non-axisymmetric endwall design. As noted earlier, three-dimensional endwall contours in the published literature have generally been designed through computational optimization coupled to a RANS-based solver. It would appear from the results presented here that a RANS-based contour design methodology might be sensitive to not only the variable or variables being optimized (e.g.,  $C_{SKE}$ ,  $C_{Ptot}$ ), but also to the turbulence model employed in the optimization routine. To the authors' knowledge, this is an area that has not received much attention as of yet.

### Endwall Heat Transfer Predictions

Comparisons of flat endwall heat transfer predictions to the measurements of Lynch et al. [11] are shown in Figure 10. The SST  $k-\omega$  model results in a significant overprediction of  $Nu$  in

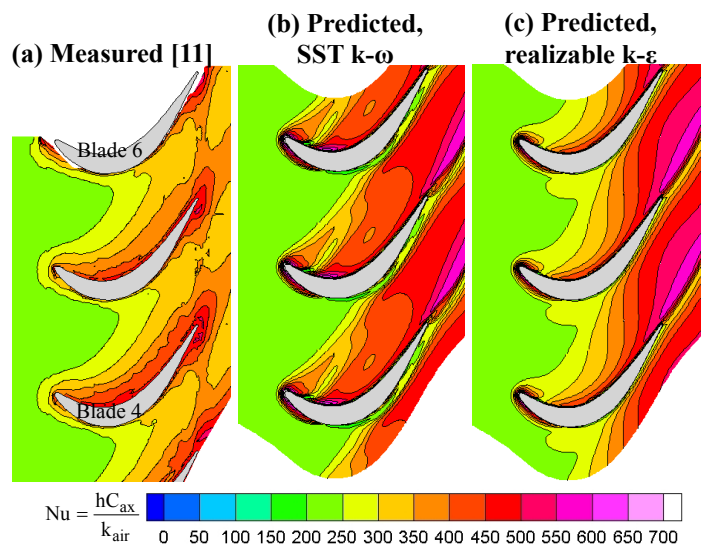


Figure 10. Flat endwall heat transfer; (a) measured [11], (b) predicted with SST  $k-\omega$ , and (c) predicted with realizable  $k-\epsilon$ .

the passage, particularly near and downstream of the trailing edge plane. There is a region of high Nu upstream of a small island of low Nu near the blade pressure side toward the leading edge in Figure 10b, which is not seen in the measurements (Figure 10a). Also, the prediction indicates low heat transfer very close to the blade suction side in the aft part of the passage. The realizable  $k-\epsilon$  prediction of flat endwall heat transfer is shown in Figure 10c. This model results in better agreement to Figure 10a in the forward portion of the passage, and does not exhibit the unique low-Nu regions seen in Figure 10b. Toward the aft portion of the passage in Figure 10c, however, the realizable  $k-\epsilon$  prediction also indicates higher Nu than was measured. The improvement of the realizable  $k-\epsilon$  over the SST  $k-\omega$  model prediction seems to be in opposition to the conclusions from the earlier flowfield comparisons, although neither turbulence model produces satisfactory heat transfer predictions over the entire endwall.

Figure 11 presents contours of heat transfer augmentation, where positive augmentation values indicate an increase in heat transfer for the contour versus the flat endwall and negative values indicate a reduction. Lynch et al. [11] noted that the contour tends to increase heat transfer near the saddle point where heat transfer is nominally low, but also reduce it near the pressure side-endwall junction where heat transfer is nominally high. These two effects are somewhat reproduced in the SST  $k-\omega$  prediction in Figure 11b, although there are some notable differences. The magnitude of heat transfer augmentation around the saddle point is significantly higher than the measured augmentation in Figure 11a. Also, the SST  $k-\omega$  model predicts larger reductions in contoured endwall heat transfer (large negative augmentation values) near the pressure side than is indicated by the measurements in Figure 11a. The region of large negative augmentation values in Figure 11b does not persist near the pressure side in the aft portion of the passage, but instead crosses the passage toward the suction side.

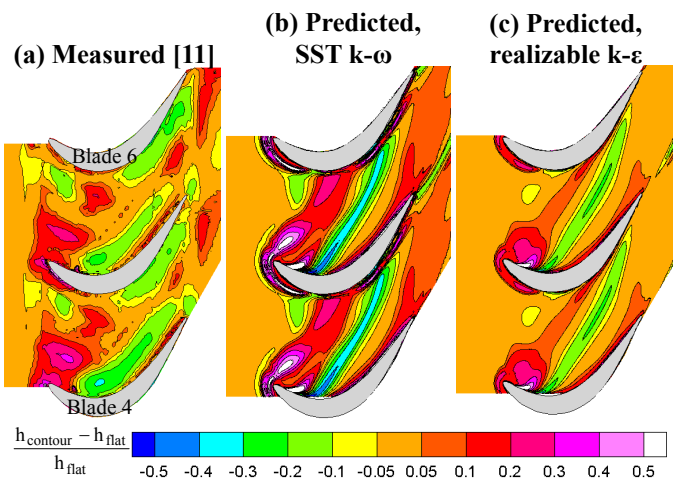


Figure 11. Endwall heat transfer augmentation; (a) measured [11], (b) predicted with SST  $k-\omega$ , and (c) predicted with realizable  $k-\epsilon$ .

Heat transfer augmentation with the realizable  $k-\epsilon$  model in Figure 11c agrees fairly well with the measurements (Figure 11a), particularly regarding the magnitudes of augmentation in the saddle point region and in the region of heat transfer reduction near the pressure side. Like the SST  $k-\omega$  prediction, however, the heat transfer reduction region near the pressure side is not as large or as close to the blade-endwall junction as is indicated in the measurements.

Line plots of heat transfer augmentation in Figure 12 were created by extracting data from Figure 11 along an inviscid streamline passing through a point located 25% of the pitch ( $0.25P$ ) from the blade leading edge in the pitch direction. The extracted data and an inset showing the  $0.25P$  streamline are shown in Figure 12. The  $0.25P$  streamline passes through the region of high heat transfer augmentation near the saddle point, as well as through the region of heat transfer reduction near the pressure side. Note that the magnitude of augmentation around the saddle point ( $X/C_{ax} \approx 0.15$ ) is overpredicted by the SST  $k-\omega$  model but underpredicted by the realizable  $k-\epsilon$  model, although both models capture the axial location of the peak augmentation. Unfortunately, the location of the largest heat transfer reduction (large negative augmentation values) beyond  $X/C_{ax} = 0.4$  in Figure 12 is not as well-predicted, with the measurements indicating that this region is spread out nearly to the trailing edge plane. The discrepancy in the predictions downstream of  $X/C_{ax} = 0.4$  is not unexpected given the poor agreement between the predicted and measured flat endwall heat transfer in the aft portion of the passage in Figure 10. This mis-prediction of the augmentation, however, could conceivably affect the optimal shape for an endwall design that attempts to incorporate endwall heat transfer as an optimization variable.

### Film-Cooling Measurements and Predictions

Measurements of flat endwall adiabatic film-cooling effectiveness for two average ideal blowing ratios ( $\overline{M}_{ideal}$ ) are

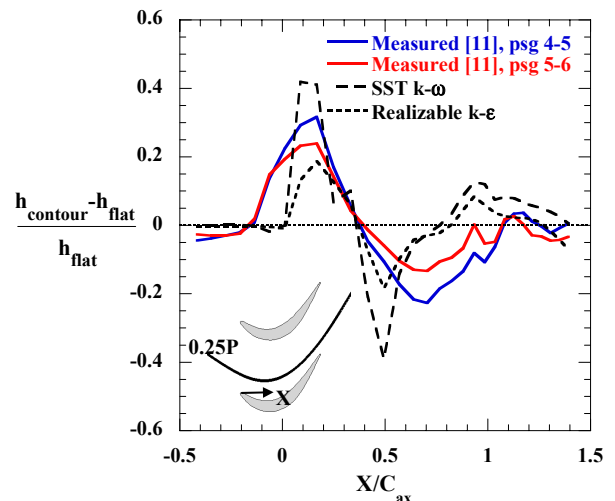


Figure 12. Heat transfer augmentation for the contoured versus flat endwall, extracted along an inviscid streamline passing through  $0.25P$ .

presented in Figures 13a-b. The influence of the cross-passage flow near the endwall is apparent in the sweeping of the coolant from the pressure to suction side, which provides some coverage over the aft portion of the passage. In Figure 13a, holes 3-5 toward the trailing edge appear to be providing more endwall cooling than holes 1 and 2. The exits of holes 1 and 2 are located in a region of higher pressure relative to the exits of holes 3-5, and thus for a given plenum total pressure, more massflow is ejected through the downstream holes where the pressure differential is larger. In Figure 13b, nearly all of the jets lift off the endwall at the average ideal blowing ratio of 2.0.

Based on the close comparison of the SST  $k-\omega$  turbulence model to the measured exit flowfield, it was selected in this study for predictions of endwall adiabatic effectiveness. The predictions for the flat endwall over a range of  $\overline{M}_{ideal}$  are shown in Figure 13c-d. The trend of coolant sweeping from the pressure to suction side is visible in the predictions, and Figure

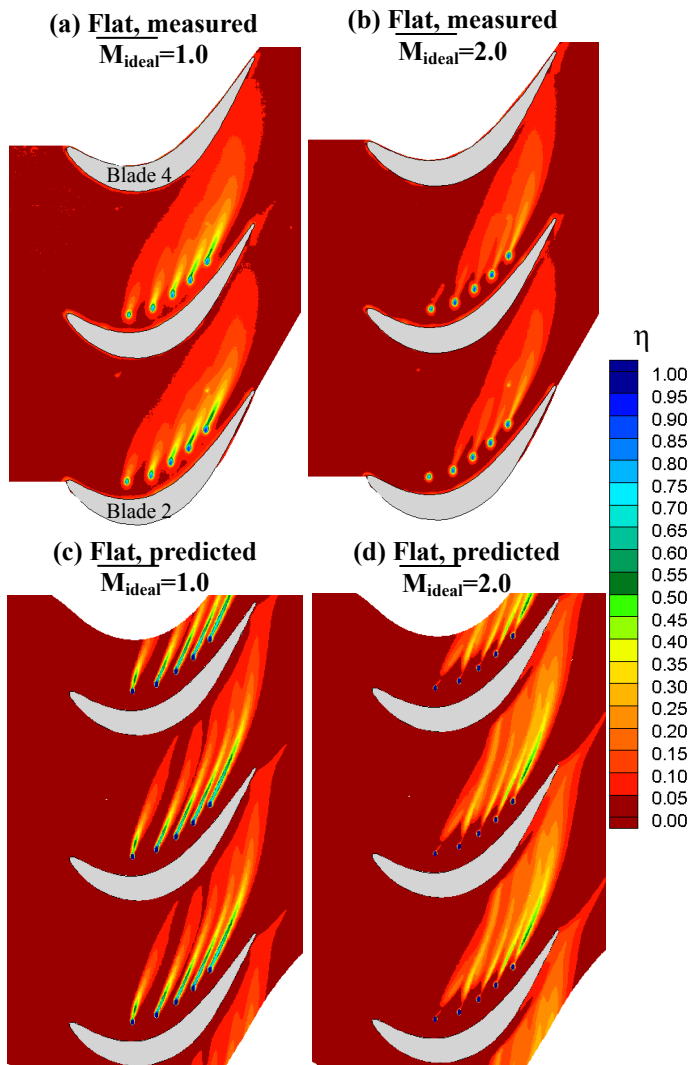


Figure 13. Flat endwall film-cooling effectiveness measurements (a-b), and predictions (c-d) using the SST  $k-\omega$  model.

13d also indicates jet lift-off for  $\overline{M}_{ideal}=2.0$ . However, jet spreading appears to be underpredicted, while peak (centerline) effectiveness is overpredicted. This is a common problem for two-equation models ([32], [33]).

Film-cooling effectiveness values downstream of hole 3 were extracted from the contour plots in Figure 13 to provide quantitative comparisons in Figures 14 and 15. These figures contain plots of maximum and laterally-averaged effectiveness along the jet direction. Since the jet trajectory downstream of hole 3 curves slightly as it moves toward the suction side, the abscissa of Figures 14 and 15 is streamwise distance downstream of the hole exit along the direction of maximum effectiveness, normalized by the hole diameter. The extent of lateral averaging in Figure 15 was limited to half of the hole pitch (pitch $\approx$ 4d) on either side of hole 3.

In Figure 14, maximum effectiveness is significantly overpredicted downstream of hole 3 for  $\overline{M}_{ideal}=1.0$ . For the

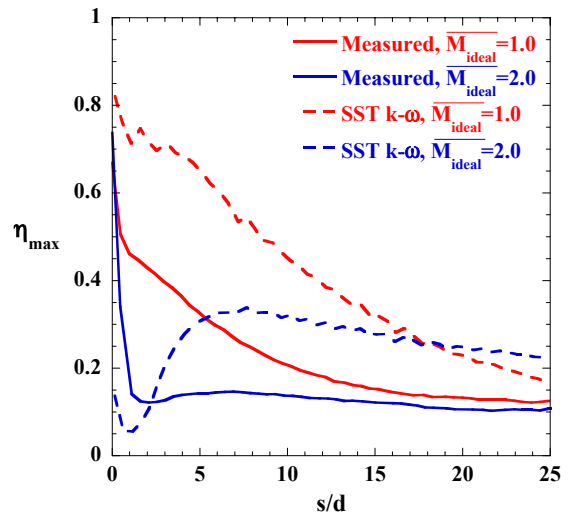


Figure 14. Maximum effectiveness downstream of hole 3, for the flat endwall.

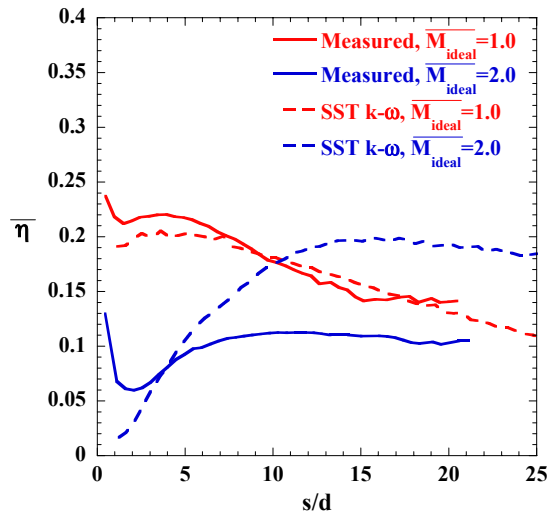
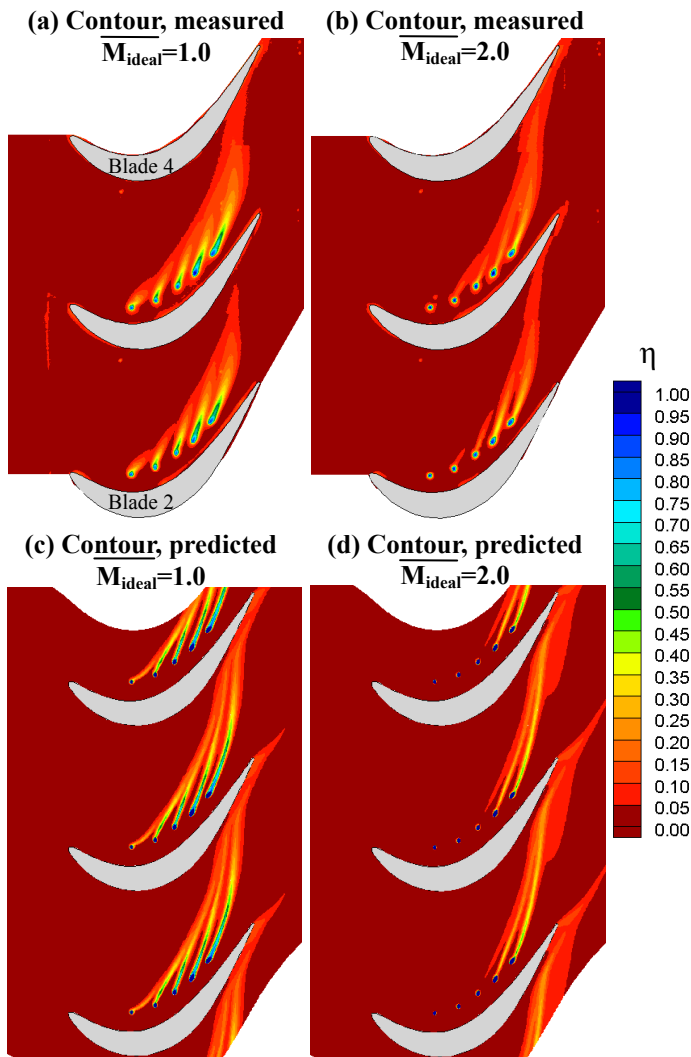


Figure 15. Laterally-averaged effectiveness downstream of hole 3, for the flat endwall.



**Figure 16. Contoured endwall film-cooling effectiveness measurements (a-b) and predictions (c-d) using the SST  $k-\omega$  model.**

highest blowing ratio, the prediction indicates better jet reattachment than was seen in the experiment. Figure 15 shows good agreement in laterally-averaged effectiveness, however, for the average ideal blowing ratio of 1.0. The laterally-averaged effectiveness of the detached jet at  $\overline{M}_{ideal}=2.0$  is not accurately simulated, with the prediction indicating much higher average effectiveness downstream of  $s/d=5$ . The performance of the SST  $k-\omega$  model for maximum and laterally-averaged effectiveness is consistent with simulations of film-cooling presented in the literature ([20], [34]).

The contoured endwall film-cooling measurements are shown in Figures 16a-b. Recall that holes 1 and 2 were required to have surface inclination angles of  $80^\circ$  and  $60^\circ$  due to manufacturing considerations so jet blow-off is expected. As the average ideal blowing ratio increases to  $\overline{M}_{ideal}=2.0$ , all of the jets have so much momentum that they detach from the surface.

Comparisons of the contoured endwall film coverage (Figures 16a-b) to the flat endwall measurements (Figures 13a-b) indicate that, in general, the cooling coverage is less spread out across an endwall with a three-dimensional contour. Furthermore, cooling jets from holes 1 and 2 in the contoured endwall are more aligned with the inviscid flow direction than the corresponding jets on the flat endwall. The effect of the contour ridge in reducing cross-passage flow has also resulted in a tendency to limit the spread of coolant across the passage. This is an important point for a designer to consider when developing a film-cooling pattern, since the development might be based off of previous experience with flat endwalls.

Contoured endwall film cooling predictions in Figures 16c-d reproduce the measured endwall coverage pattern indicated in Figures 16a-b. As was seen for the flat endwall, jet spreading and maximum effectiveness were under- and overpredicted, respectively. In Figure 17, laterally-averaged effectiveness downstream of hole 3 for  $\overline{M}_{ideal}=1.0$  is plotted for the flat and contoured endwall measurements, as well as for their respective predictions. Note that hole 3 has a surface inclination angle of  $40^\circ$  for the flat endwall and  $45^\circ$  for the contoured endwall. Figure 17 shows that the contour has reduced effectiveness compared to the flat endwall, although a direct comparison is somewhat complicated by the difference in surface inclination angles. The prediction of laterally-averaged effectiveness for the contour is higher than the experiment. This may be due to a mis-prediction of the near-wall flowfield with endwall contouring in this region; recall in Figure 11b that the heat transfer augmentation was also mis-predicted near the pressure side-endwall junction.

## CONCLUSIONS

Computational simulations of a flat and non-axisymmetric contoured endwall were performed with a steady RANS code and compared to exit flowfield, endwall heat transfer, and endwall film cooling effectiveness measurements. The

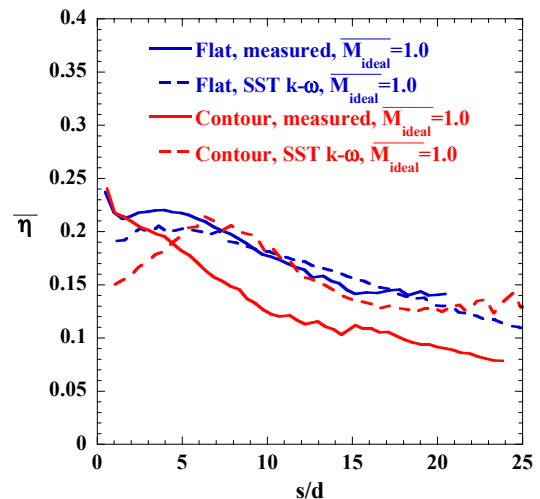


**Figure 17. Laterally-averaged effectiveness downstream of hole 3, for the contoured versus flat endwalls.**

computations compared two turbulence models (SST  $k-\omega$  and realizable  $k-\epsilon$ ) for predictions of the exit flowfield and endwall heat transfer. For the SST  $k-\omega$  model, predicted secondary kinetic energy agreed well with flat endwall measurements above 8% span but underpredicted  $C_{SKE}$  below that span. Predictions for the contoured endwall were not quite as good as for the flat endwall, suggesting that RANS models may not be fully capturing the physics of contouring. Total pressure loss predictions of the flat and contoured endwalls indicated similar loss structures but the magnitude of loss was overpredicted. The realizable  $k-\epsilon$  model significantly underpredicted secondary kinetic energy and did not accurately capture either the structure or magnitude of total pressure loss.

The SST  $k-\omega$  model and the realizable  $k-\epsilon$  model significantly overpredicted flat endwall heat transfer in the passage. Measured heat transfer for a contoured versus flat endwall was augmented around the saddle point but reduced near the pressure side. These trends were reproduced in the SST  $k-\omega$  and realizable  $k-\epsilon$  simulations, although the level of augmentation was overpredicted by the SST  $k-\omega$  model.

Film cooling holes were placed in the region of high heat transfer near the pressure side-endwall junction for both the flat and contoured endwall geometries. Measured effectiveness illustrated the effect of the cross-passage flow on the spreading of coolant over the flat endwall, and the tendency for jet lift-off at high blowing ratios. Predictions for the flat endwall using the SST  $k-\omega$  model replicated these trends, with good agreement in laterally-averaged effectiveness. The application of endwall contouring was shown to reduce the spreading of coolant across the endwall, due to the reduction in cross-passage flow with a contour. Effectiveness simulations duplicated the measured trends, but overpredicted laterally-averaged effectiveness.

Overall, the steady RANS simulations demonstrated good predictions of secondary kinetic energy and endwall film-cooling effectiveness, but poor predictions of total pressure loss and endwall heat transfer. Improving the latter appears to be the next major hurdle in increasing axial turbine efficiency and durability through fully optimal aerodynamic and thermal designs.

## ACKNOWLEDGMENTS

The authors gratefully acknowledge United Technologies—Pratt & Whitney for their support of this work, and Eunice Allen-Bradley for performing the endwall contour design. We also would like to thank Daniel Knezevici and Dr. Steen Sjolander for providing us with a copy of the experimental dataset for the cascade exit flowfield.

## REFERENCES

[1] Harvey, N.W., Rose, M.G., Taylor, M.D., Shahpar, S., Hartland, J., and Gregory-Smith, D., 2000, "Non-Axisymmetric Turbine End Wall Design: Part I—Three-Dimensional Linear Design System," *J. of Turbomachinery*, Vol. 122, pp. 278-285.

[2] Hartland, J., Gregory-Smith, D., Harvey, N.W., and Rose, M.G., 2000, "Non-Axisymmetric Turbine End Wall Design: Part II—Experimental Validation," *J. of Turbomachinery*, Vol. 122, pp. 286-293.

[3] Nagel, M.G. and Baier, R.D., 2005, "Experimentally Verified Numerical Optimization of a Three-Dimensional Parameterized Turbine Vane with Nonaxisymmetric Endwalls," *J. of Turbomachinery*, Vol. 127, pp. 380-387.

[4] Germain, T., Nagel, M., Raab, I., Scheupbach, P., Abhari, R.S., and Rose, M., 2008, "Improving Efficiency of a High-Work Turbine Using Non-Axisymmetric Endwalls Part I: Endwall Design and Performance," ASME Paper GT2008-50469.

[5] Scheupbach, P., Abhari, R.S., Rose, M., Germain, T., Raab, I., and Gier, J., 2008, "Improving Efficiency of a High-Work Turbine Using Non-Axisymmetric Endwalls Part II: Time-Resolved Flow Physics," ASME Paper GT2008-50470.

[6] Praisner, T.J., Allen-Bradley, E., Grover, E.A., Knezevici, D.Z., and Sjolander, S.A., 2007, "Application of Non-Axisymmetric Endwall Contouring to Conventional and High-Lift Airfoils," ASME Paper GT2007-27579.

[7] Knezevici, D.Z., Sjolander, S.A., Praisner, T.J., Allen-Bradley, E., and Grover, E.A., 2008, "Measurements of Secondary Losses in a Turbine Cascade with the Implementation of Non-axisymmetric Endwall Contouring," *J. of Turbomachinery*, Vol. 132, pp. 011013-1-10.

[8] Knezevici, D.Z., Sjolander, S.A., Praisner, T.J., Allen-Bradley, E., and Grover, E.A., 2009, "Measurements of Secondary Losses in a High-Lift Front-Loaded Turbine Cascade with the Implementation of Non-axisymmetric Endwall Contouring," ASME Paper GT2009-59677.

[9] Saha, A.K. and Acharya, S., 2008, "Computations of Turbulent Flow and Heat Transfer Through a Three-Dimensional Nonaxisymmetric Blade Passage," *J. of Turbomachinery*, Vol. 130, pp. 031008-1-10.

[10] Mahmood, G.I. and Acharya, S., 2007, "Measured Endwall Flow and Passage Heat Transfer in a Linear Blade Passage with Endwall and Leading Edge Modifications," ASME Paper GT2007-28179.

[11] Lynch, S.P., Sundaram, N., Thole, K.A., Kohli, A., and Lehane, C., 2009, "Heat Transfer for a Turbine Blade with Non-Axisymmetric Endwall Contouring," ASME paper GT2009-60185.

[12] Okita, Y. and Nakamata, C., 2008, "Computational Predictions of Endwall Film Cooling for a Turbine Nozzle Vane with an Asymmetric Contoured Passage," ASME Paper GT2008-50878.

[13] Gustafson, R., Mahmood, G.I., and Acharya, S., 2007, "Flowfield in a Film-Cooled Three-Dimensional Endwall Passage: Aerodynamic Measurements," ASME Paper GT2007-28154.

[14] Mahmood, G.I., Gustafson, R., and Acharya, S., 2009, "Flow Dynamics and Film Cooling Effectiveness on a

Non-Axisymmetric Contour Endwall in a Two-Dimensional Cascade Passage,” ASME Paper GT2009-60236.

- [15] ANSYS FLUENT (version 12.0.16), 2009, ANSYS Inc., Canonsburg, PA.
- [16] Menter, F.R., 1994, “Two-Equation Eddy Viscosity Turbulence Models for Engineering Applications,” *AIAA J.*, Vol. 32 (No. 8), pp. 1598-1605.
- [17] Schwänen, M. and Duggleby, A., 2009, “Identifying Inefficiencies in Unsteady Pin-Fin Heat Transfer,” ASME Paper GT2009-60219.
- [18] Snedden, G., Dunn, D., Ingram, G., and Gregory-Smith, D., 2009, “The Application of Non-Axisymmetric Endwall Contouring in a Single-Stage Rotating Turbine,” ASME Paper GT2009-59169.
- [19] Shih, T.-H., Liou, W.W., Shabbir, A., Yang, Z., and Zhu, J., 1995, “A New  $k$ - $\epsilon$  Eddy-Viscosity Model for High Reynolds Number Turbulent Flows—Model Development and Validation,” *Computers and Fluids*, Vol. 24 (No. 3), pp. 227-238.
- [20] Harrison, K.L. and Bogard, D.G., 2008, “Comparison of RANS Turbulence Models for Prediction of Film Cooling Performance,” ASME Paper GT2008-51423.
- [21] Yang, H., Acharya, S., Ekkad, S., Prakash, C., and Bunker, R., 2002, “Flow and Heat Transfer Predictions for a Flat-Tip Turbine Blade,” ASME Paper GT2002-30190.
- [22] Hermanson, K., Kern, S., Picker, G., and Parneix, S., 2003, “Predictions of External Heat Transfer for Turbine Vanes and Blades with Secondary Flowfields,” *J. of Turbomachinery*, Vol. 125, pp. 107-113.
- [23] ANSYS ICEM CFD (version 11.0), 2009, ANSYS Inc., Canonsburg, PA.
- [24] Crawford, M.E., 2009, TEXSTAN (academic version), University of Texas, Austin, TX.
- [25] Kays, W. M. and Crawford, M. E., 1980, *Convective Heat and Mass Transfer* (2<sup>nd</sup> ed.), McGraw-Hill, New York, pp. 216-217.
- [26] Bons, J.P., Sondergaard, R., and Rivir, R. B., 2001, “Turbine Separation Control Using Pulsed Vortex Generator Jets,” *J. of Turbomachinery*, Vol. 123, pp. 198-206.
- [27] McAuliffe, B.R. and Sjolander, S.A., 2004, “Active Flow Control Using Steady Blowing for a Low-Pressure Turbine Cascade,” *J. of Turbomachinery*, Vol. 126, pp. 560-569.
- [28] Popovic, I., Zhu, J., Dai, W., Sjolander, S.A., Praisner, T.J. and Grover, E.A., 2006, “Aerodynamics of a Family of Three Highly Loaded Low-Pressure Turbine Airfoils: Measured Effects of Reynolds Number and Turbulence Intensity in Steady Flow,” ASME Paper GT2006-91271.
- [29] Zoric, T., Popovic, I., Sjolander, S.A., Praisner, T., and Grover, E., 2007, “Comparative Investigation of Three Highly-Loaded LP Turbine Airfoils: Part I—Measured Profile and Secondary Losses at Design Incidence,” ASME Paper GT2007-27537.
- [30] Moffat, R. J., 1988, “Describing the Uncertainties in Experimental Results,” *Experimental Thermal and Fluid Science*, Vol. 1, pp. 3-17.
- [31] Cleak, J.G.E. and Gregory-Smith, D.G., 1992, “Turbulence Modeling for Secondary Flow Prediction in a Turbine Cascade,” *J. of Turbomachinery*, Vol. 114, pp. 590-598.
- [32] Walters, D.K. and Leylek, J.H., 2000, “A Detailed Analysis of Film-Cooling Physics: Part I—Streamwise Injection with Cylindrical Holes,” *J. of Turbomachinery*, Vol. 122, pp. 102-112.
- [33] Bogard, D.G. and Thole, K.A., 2006, “Gas Turbine Film Cooling,” *J. of Propulsion and Power*, Vol. 22 (No. 2), pp. 249-270.
- [34] Na, S., Zhu, B., Bryden, M., and Shih, T.I-P., 2006, “CFD Analysis of Film-Cooling,” AIAA Paper AIAA2006-0022.